



Hydrothermal Fe–Si–Mn oxide deposits from the Central and South Valu Fa Ridge, Lau Basin

Zhilei Sun^{a,b,c}, Huaiyang Zhou^{a,d,*}, Qunhui Yang^d, Zhixue Sun^e, Shenxu Bao^f, Huiqiang Yao^g

^a Guangzhou Institute of Geochemistry, Chinese Academy of Sciences, Guangzhou 510640, China

^b Graduate University of Chinese Academy of Sciences, 100049, Beijing, China

^c Key Laboratory of Marine Hydrocarbon Resources and Environmental Geology, Ministry of Land and Resources, Qingdao 266071, China

^d National Key Lab of Marine Geology, Tongji University, Shanghai 200092, China.

^e School of Petroleum Engineering, China University of Petroleum, Qingdao 266555, China

^f Wuhan University of Technology, Wuhan 430070, China

^g Guangzhou Marine Geological Survey, Guangzhou 510075, China

ARTICLE INFO

Article history:

Received 12 May 2010

Accepted 9 April 2011

Available online 16 April 2011

Editorial handling by R. Fuge

ABSTRACT

A series of samples from the Hine Hina hydrothermal field (HHF) and the Mariner hydrothermal field (MHF) in the Central and Southern Valu Fa Ridge (VFR), Lau Basin were examined to explain the source origin and formation of the hydrothermal Fe–Si–Mn oxide deposits. The mineralogy was studied by X-ray diffraction (XRD), scanning electron microscopy (SEM), Mössbauer spectroscopy, and energy-dispersive spectroscopy (EDS). For the Fe–Mn oxide crusts in the HHF, varying amounts of volcanic fragments and some seawater contributions were recognized, along with higher concentrations of Mn, Al, Co, Ni, Zn, Sr, Mo, elevated Σ REE and negative Ce anomalies. In contrast, the Si-rich oxide samples of the MHF were enriched in Cu, Pb and Ba, indicative of proximity to a hydrothermal jet. Moreover, conductive cooling of hydrothermal fluid evoked the Si-rich deposit formation in the MHF. The Sr, Nd and Pb isotope data provided further constraints regarding the source and formation of the Fe–Si–Mn deposits in the VFR by showing that the samples of the HHF are a mixture of three components, namely, hydrothermal fluid, seawater and volcanic materials, whereas the samples of the MHF were dominated by hydrothermal fluids. The seawater had a minor influence on the Nd isotope data, and the Pb isotope data exhibited a close association with the substrate rock and preformed volcanoclastic layers in this area. The occurrence of relatively high Mn/Fe ratios in the hydrothermal deposits of this area may be a good indicator of the propagating activities of the VFR over geological time.

© 2011 Elsevier Ltd. All rights reserved.

1. Introduction

Hydrothermal Fe–Si–Mn oxide deposits (including Mn-rich crusts) are important constituents of modern ocean-floor deposits in various geological settings, such as mid-ocean ridges (Binns et al., 1993; Hekinian et al., 1993; Kennedy et al., 2003; Hrischeva and Scott, 2007; Dekov et al., 2010), back-arc basins (Fouquet et al., 1993; Iizasa et al., 1998; Dekov and Savelli, 2004; Kato et al., 2009), intra-plate seamounts (Alt, 1988; Boyd and Scott, 1999; Dekov et al., 2009), active volcanic arcs (Hein et al., 2008), and occasionally, shallow water environments (Pichler and Veizer, 1999).

Besides the plume fallout, corrosion and mass wasting of metal sulfides, the hydrothermal low-temperature diffuse fluid is also recognized as a common source of Fe–Si–Mn oxide deposits

* Corresponding author at: National Key Lab of Marine Geology, Tongji University, Shanghai 200092, China. Fax: +86 21 65987615.

E-mail addresses: zhouhy@tongji.edu.cn (H. Zhou), zhileisun@yahoo.net (Z. Sun).

(e.g., Boyd and Scott, 1999; Hein et al., 2008; Dekov et al., 2009). Due to the pervasive distribution in the hydrothermal system, the low-temperature diffuse flow is much more certain and effective for indicating the intensities, extents and directions of hydrothermal ore-forming processes. The Fe–Si–Mn oxide formed by diffuse flow can thus provide valuable information regarding the development and migration of hydrothermal activities, deepen understanding of the entire process of ore deposition and even be a useful tool for tracing ancient hydrothermal systems (Pichler and Veizer, 1999; Gurvich, 2006; Hrischeva and Scott, 2007). This paper reports on the mineralogy, geochemistry (major and trace elements) and Sr, Nd and Pb isotopes of diffuse flow Fe–Si–Mn deposits collected from two hydrothermal fields along the same ridge (now in different developmental stages). The aim is to explain the origin of the deposits that are currently accumulating near the two active hydrothermal fields. The factors controlling the hydrothermal deposits formed in diffuse flow-dominated areas of the hydrothermal fields are also discussed.

2. Geological setting

The Lau Basin is a wedge-shaped, back-arc basin located in the SW Pacific Ocean, just west of the Tonga Trench. About 5.5 Ma ago, true back-arc spreading began and propagated southwards (Hawkins, 1995). Currently, the Lau Basin is composed of three major active spreading ridges: the Central Lau Spreading Center (CLSC), the Eastern Lau Spreading Center (ELSC), and the southernmost area (south of 21°20'S), which is referred to as the Valu Fa Ridge (VFR; Jenner et al., 1987; Sinha, 1995) (Fig. 1A). The VFR is an active, back-arc spreading center of the Lau Basin (Morton and Sleep, 1985) and is spreading at a rate of 60 mm/a based on magnetic anomaly identification (Morton and Pohl, 1990). It extends for at least 165 km in length, is 5–6 km wide and has ridge flanks rising about 600 m above the surrounding seafloor. At about 22°45'S, it propagates southward into the Miocene island arc crust (Wiedicke and Collier, 1993; Taylor et al., 1996). Geophysical studies suggest that the VFR is divided into three ridge sections: the southern, central and northern VFR (SVFR, CVFR and NVFR, respectively) (Von Stackelberg et al., 1988). The CVFR is underlain by a steady axial magma chamber that extends 20 km along a profile recorded along the entire axis of the VFR (from 22°10'S to 22°30'S according to seismic data) (Collier and Sinha, 1990, 1992). The top of the magma reservoir is considered to be 2–3 km wide and located 3.2 km below the seafloor, which is relatively deep compared to reservoirs found along mid-ocean ridges (e.g., 1.2–2.4 km beneath the East Pacific Rise, Detrick et al., 1987).

The formation of several hydrothermal fields has been triggered at different periods by the southward expansion movement of the VFR. These fields are, from north to south, the Tui Malila, White Church, Vai Lili, Mariner and Hina Hine hydrothermal fields (Fouquet et al., 1991, 1993; Ferrini et al., 2008; Takai et al., 2008). Based on previous findings (Fouquet et al., 1993), three different volcanic and tectonic stages are recognized along the VFR. The SVFR (including the HHF) is in the volcanic stage, with pervasive diffuse

discharge (~40 °C; Fouquet et al., 1991; Lécuyer et al., 1999) percolating through highly porous volcanoclastic material and producing extensive Fe–Mn oxide crusts (Fouquet et al., 1993). At this stage, there are no major faults and the upper part of the discharge is diffuse and involves significant mixing with seawater. The system produced widespread low-temperature discharge and associated Fe–Mn oxide deposits at the surface, representing the first stage of hydrothermal activity. The Fe–Mn oxide crusts and the hydrothermally cemented sediments (with fossil ripple marks) progressively led to a near-surface sealing of the hydrothermal system. The CVFR (including the MHF and the Vai Lili hydrothermal field) is now in the volcanic/tectonic stage, with numerous black and white smokers discharging up to 400 °C fluids in the Vai Lili field and ~365 °C fluids in the MHF (Takai et al., 2008). However, diffuse discharges are still present in some limited areas (Fouquet et al., 1993; Lécuyer et al., 1999). The MHF is one of the newly discovered hydrothermal systems located at the northern end of the CVFR. Hydrothermal activity at the MHF is primarily associated with vent pinnacles emanating hot fluids from close to their bases and part way up their sides (Tivey et al., 2005). Visual observations show that some localized areas of lower-temperature flow, from tabular, squat edifices are present E–NE of the hydrothermal pinnacles.

3. Samples and methods

Sampling was performed with a TV-guided grab at several hydrothermal fields along the SVFR and the CVFR during the hydrothermal activity expedition of R/V DaYang YiHao in May 2007. The main sampling sites were TVG5 and TVG6 in the HHF, and TVG9 in the MHF. The details of bathymetry and the locations of sampling sites at the HHF and the MHF are shown in Fig. 1B. The samples from the TVG5 and TVG6 stations are crusts of sooty, black material that are semi-consolidated, slightly laminated, coated by a thin film (millimeter- to centimeter-scale) and contain various

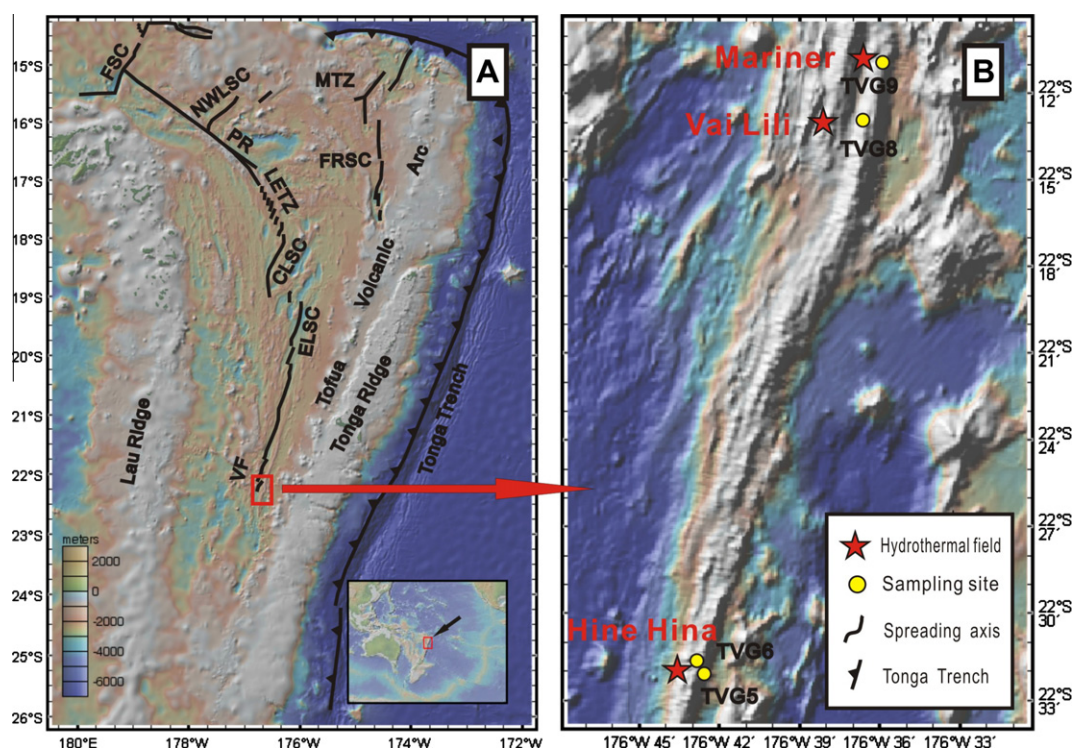


Fig. 1. Bathymetry of the Lau Basin (A) and Central-Northern VFR (B) from the GeoMapApp website (<http://www.geomapapp.org/>) and sampling sites of this study. The horizontal axis is longitude (°W) with the vertical axis is latitude (°S).



Fig. 2. Bottom photographs of Fe–Si–Mn oxides and patchy nontronites in the VFR taken with TV-guide crab. A. Fe–Mn oxide crust from the HHF (TVG5 Site) showing laminated layers of various colors. B. Fe–Mn oxide crust from the HHF (TVG6 Site); C. Fe–Si oxide precipitates from the MHF (TVG9 Site), the green patch is nontronite.

amounts of volcanic shards (Fig. 2A and B). The upper black layers and the lower yellow layers were sampled; the black subsamples are labeled “B” at the end of the analysis number, while the yellow subsamples are labeled “Y”. The TVG9 samples showed no laminated textures and are mainly bright yellow to orange–yellow loose sediments with some greenish patches in them (Fig. 2C). The samples were split into several subsamples based on macroscopic differences. A volcanic fragment sample (L5-4D) was obtained by sieving from the bulk sample of TVG5. Detailed information for all subsamples is reported in Table 1.

The bulk mineralogy of a powdered specimen was determined by X-ray diffraction (XRD) using a Phillips PW1050 diffractometer (Cu K α radiation, Ni filter, 40 kV, 40 mA, scan capabilities from 2° to 90° 2 θ , scan velocity of 1° 2 θ /min). Scanning electron microscope (SEM) observations were made on C-coated fragments of freeze-dried bulk samples using a FEI Quant 400 electron microscope. Semi-quantitative chemical analyses were undertaken using energy-dispersive spectroscopy (EDS), performed in real time at an accelerating voltage of 20 keV for 100 s. ^{57}Fe Mössbauer spectroscopy was carried out on powdered samples using a conventional Mössbauer spectrometer (Wissel) in transmission geometry at room temperature (RT). A $^{57}\text{Co/Rh}$ γ -radiation source of 3.6×10^9 Bq activity was used and the isomer shifts are reported relative to α -Fe. The resulting Mössbauer spectra were fitted with doublets of Lorentzian peaks using a sum-of-squares minimization algorithm within the Mosswin3.0 code platform. The major elements were quantitatively determined by inductively-coupled plasma optical emission spectrometry (ICP-OES) with an analytical precision within $\pm 5\%$. Trace elements were determined by inductively-coupled plasma mass spectrometry (ICP-MS) from a separate 0.5 g split digested in aqua regia for each sample, and the external precision for the analyses was within $\pm 5\%$.

For the Sr and Nd isotope analyses, the samples were dissolved in HF–HNO $_3$ and Sr and Nd were purified using standard chromatographic techniques.

Isotope measurements were performed with a Nu-Plasma MC-ICP-MS. The Sr isotopes were acquired in a static mode using 5 Faraday collectors, and the $^{87}\text{Sr}/^{86}\text{Sr}$ ratio was corrected for mass bias using an exponential law and the value of 0.1194 for the ratio $^{86}\text{Sr}/^{88}\text{Sr}$. For Nd, all measured ratios were normalized to $^{146}\text{Nd}/^{144}\text{Nd} = 0.7219$ using an exponential law for mass-bias correction. Measured values for NBS 987 and JNd-i standards were $^{87}\text{Sr}/^{86}\text{Sr} = 0.710248 \pm 24$ (2 s, $n = 56$) and $^{143}\text{Nd}/^{144}\text{Nd} = 0.512106 \pm 10$ (2 s, $n = 28$), respectively. Lead isotopic ratios were measured in static mode with Nu Plasma MC-ICP-MS, and the results were corrected for mass fractionation by $\sim 0.13\%$ amu $^{-1}$, based on replicate measurements of NBS 981 ($n = 180$). The analytical precision of the measurements inferred from a large number of data on NBS981 was less than $\pm 0.02\%$ amu $^{-1}$. Total procedure blank was less than 80 pg Pb. For details of the analytical procedures and techniques, see Woodhead et al., 1995. During sampling, volcanic fragments were found to be pervasive in samples from HHF, so some samples were wet-sieved through a 0.178-mm mesh to collect the shards. The residues on the sieves were treated with 3 wt% HCl to remove carbonates, and they were rinsed with deionized water several times. The black shards (sample number L5-4D) were then analyzed together with the hydrothermal deposit samples to obtain exact information about the volcanic fragments.

4. Results

4.1. Lithology and mineralogy

The results of the combined XRD, SEM and EDS analyses suggest that all samples except for L5-4D contained high contents (generally ≥ 50 wt%) of amorphous minerals; however, there were distinct differences in the mineralogy and mineral assemblages of the two fields. In the HHF, the black crust layers were identified

Table 1
Investigated Fe–Si–Mn oxide samples from the HHF and MHF, Lau Basin.

Field	Sample	TVG No.	Lat. (S)	Long. (W)	Depth (m)	Sample description	Mineral composition ^a
Hine Hina	L5-1	5	22°32'01"	176°42'39"	1906	Yellow, loose sediments	Op, Fh
Hine Hina	L5-2B	5	22°32'01"	176°42'39"	1906	Sooty, semi-consolidated crust	Sa, Fh, B, Fh, Op
Hine Hina	L5-2Y	5	22°32'01"	176°42'39"	1906	Yellow, layered, semi-consolidated	Op, Fh
Hine Hina	L5-3	5	22°32'01"	176°42'39"	1906	Red to brown loose sediments	Op, Fh
Hine Hina	L5-4D	5	22°32'01"	176°42'39"	1906	Black fragments sieved from bulk sample	–
Hine Hina	L6-1	6	22°31'54"	176°42'56"	1877	Brown, layered, loose to semi-consolidated	Op, Fh
Hine Hina	L6-2B	6	22°31'54"	176°42'56"	1877	Black-red crust	Op, Fh, B, V, Sa
Hine Hina	L6-2Y	6	22°31'54"	176°42'56"	1877	Yellow, loose sediments	Op, Fh
Mariner	L9-1	9	22°10'53"	176°36'06"	1922	Yellow, thick, non-layered sediments	Op, Fh
Mariner	L9-2P	9	22°10'53"	176°36'06"	1922	Greenish, patchy	Op, Fh
Mariner	L9-2Y	9	22°10'53"	176°36'06"	1922	Bright yellow, thick, loose	Op, Fh
Mariner	L9-2G	9	22°10'53"	176°36'06"	1922	Brown-yellow, thick, loose	N, Op, Fh
Mariner	L9-3	9	22°10'53"	176°36'06"	1922	Yellow, loose sediments	Op, Fh

^a (1) Op = amorphous opal, Fh = 2-line-ferrihydrate, B = birnessite, V = vernadite, Sa = saponite, N = nontronite; (2) Analytical methods: XRD, Mössbauer Spectroscopy.

as having a large contribution of birnessite, todokorite (Fig. 3A and B), and a minor contribution of vernadite (Fig. 3B). The todokorite was only found in L5-2B. The yellow layers were mainly composed of hydrous ferric oxide (HFO) and are generally characterized by diffraction patterns with d-spacing-values of 2.5 (approximately $36^\circ 2\theta$) and 1.5 Å (approximately $62^\circ 2\theta$), corresponding to 2-line-ferrihydrite (Cornell and Schwertmann, 1996). In the MHF, most samples are amorphous, showing a broad, diffuse peak with the center at about 4.0 Å (approximately $22.2^\circ 2\theta$, Fig. 3C), which is typical for opal-A ($\text{SiO}_2 \cdot n\text{H}_2\text{O}$) according to the nomenclature given by Jones and Segnit (1971). Moreover, the green patchy precipitate was identified as nontronite (Fig. 3D). Based on SEM analysis, the Mn oxides typically occur as tiny rosettes that always congregate together to form a crust (Fig. 4A and B). The opal-A occurs as aggregates of smooth globular or spheroidal morphologies (Fig. 4C), whereas the green patchy nontronite (L9-2P) displays honeycomb texture (Fig. 4D). The typical ^{57}Fe Mössbauer spectrum of nontronite is shown in Fig. 4E. In the HHF, however, only scattered nontronites were separated according to Stokes law, with all clay-size ($<2\ \mu\text{m}$) minerals comprising not more than 1.5 wt% of the bulk samples. According to the SEM and EDS analyses (Fig. 4F and G), Fe–Si oxide filaments are pervasive in both fields, and the unique structures are probably indicative of the biogenetic effects, such as the neutrophilic Fe-oxidizing bacteria (e.g., Kennedy et al., 2003; Little et al., 2004; Emerson et al., 2007).

Volcanic fragments were found in the samples from the HHF, with diameters ranging from several tens of microns to several millimeters. In contrast, however, no sign of volcanic shards was observed in the MHF. Due to the small size of these volcanic shards, the exact content cannot be assessed by relying solely on the bin-

ocular microscope. The SEM also showed that the structure of the angular volcanic shards contains obvious holes, suggesting frequent volcanic activity in this area (Fig. 4I). Moreover, minor saponite was identified by XRD and optical microscopy, it often forms the rim of the altered volcanic shards consistent with previous studies (Pichler et al., 1999).

No pelagic carbonate oozes or metal sulfide debris, which are common in metalliferous sediments formed by distal plume fallout or by mass wasting and the corrosion of metal sulfides (Metz et al., 1988; German et al., 1993; Mills et al., 1993; Hannington et al., 1998), were found in either of the two hydrothermal fields.

4.2. Bulk-rock geochemistry

4.2.1. Major and minor elements

As shown in Table 2, all the hydrothermal samples have high SiO_2 contents, with an average of 51.0 wt% ($n=12$, excluding sample L5-4D). The Fe content is higher than any other element except Si, with an average up to 19.2 wt% Fe_2O_3 . The samples of the MHF have the highest average Si contents (mean 60.7 wt%, up to 77.4 wt% SiO_2) and lower average Fe contents (mean 17.4 wt% Fe_2O_3) except for the nontronite which has the highest Fe content (34.2 wt% Fe_2O_3) of all. The samples of the HHF have higher Fe (mean 20.3 wt% Fe_2O_3) and lower Si contents (mean 43.9 wt% SiO_2) compared to samples of the MHF. Another different feature in both fields is the contents of Al and Mn. The samples of the MHF have almost no Al (mean 0.026 wt% Al_2O_3) and relatively low Mn (mean 1.84 wt% MnO), whereas the samples of the HHF contain higher Al (mean 4.37 wt%, up to 8.90 wt% Al_2O_3 , sample L5-4D excluded) and Mn (mean 5.11 wt% up to

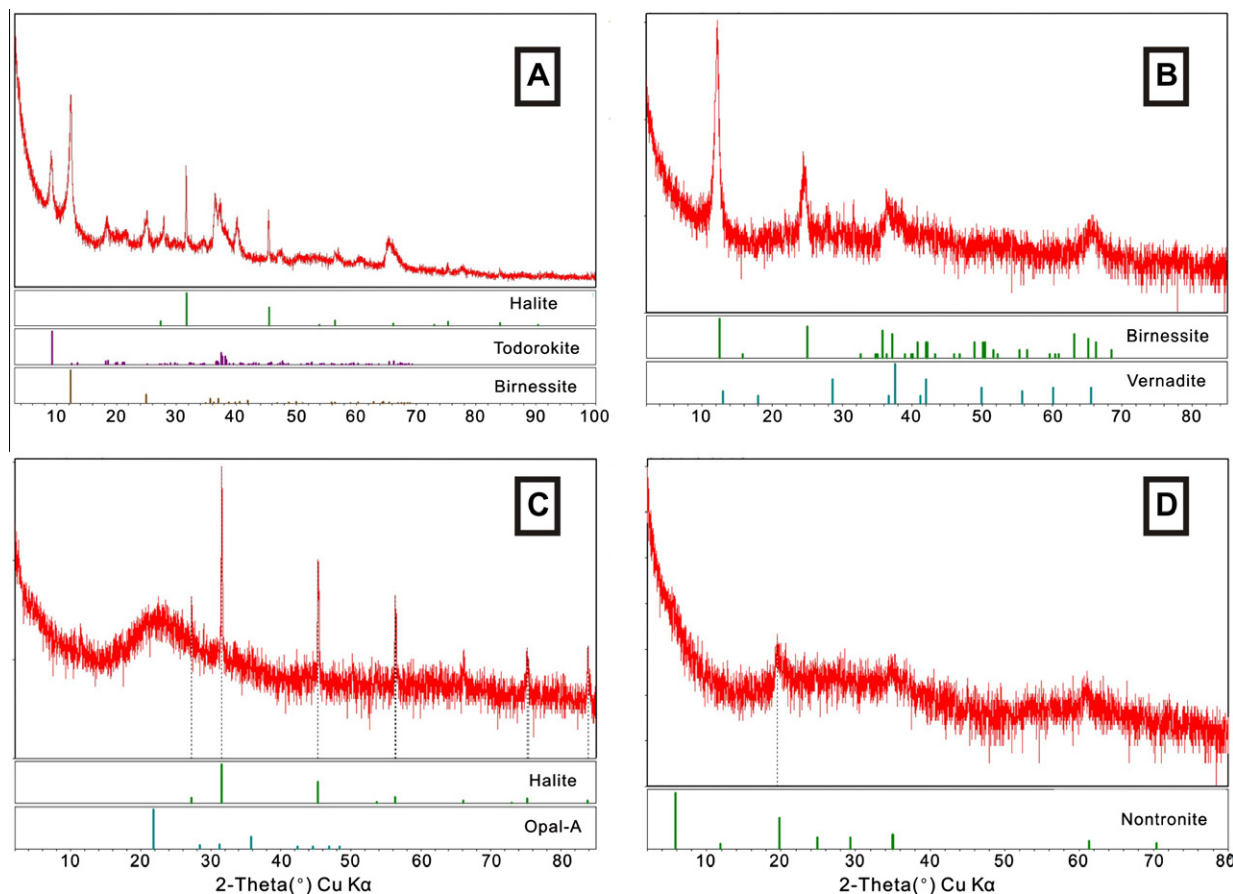


Fig. 3. XRD patterns of the Fe–Si–Mn oxide deposits from the HHF and MHF. A. Sample L5-2B from the HHF; B. Sample L6-2B from the HHF; C. Sample L9-2Y from the MHF; D. Sample L9-2P from the MHF.

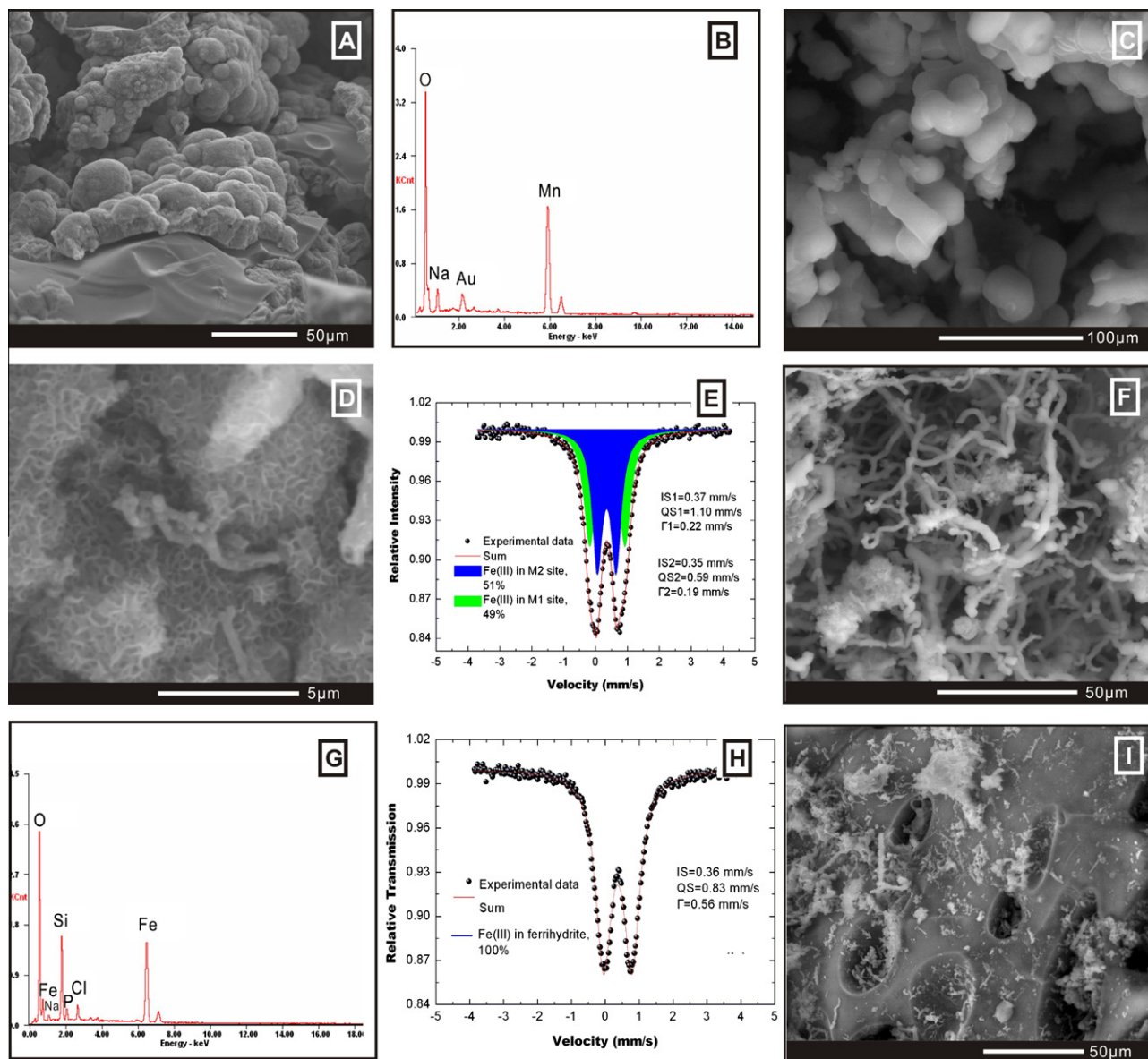


Fig. 4. SEM images, EDS and MS of hydrothermal Fe-Si-Mn oxides and nontronite in the hydrothermal field of the VFR. A. Tiny Mn oxide rosettes constitute the Mn-rich crusts. The smooth lower part is comprised of volcanic shards (sample L6-2B from TVG6 site, HHF). B. EDS spectrum of the Mn oxide rosettes in image A. C. Amorphous opal globules in sample L9-2Y from the TVG9 site. D. honeycomb-like nontronite from TVG9 (sample L9-2P). E. ^{57}Fe Mössbauer spectrum (RT) and the fitting results of nontronite in image D. F. Filamentous structure of Fe-Si oxide precipitates (sample L5-2Y, TVG5 Site, HHF). G. EDS spectrum of the Fe-Si oxide filaments in image F. H. ^{57}Fe Mössbauer spectrum (RT) and fitting results of the Fe oxide in F, showing that the iron oxide is 2-line-ferrihydrite. I. Basaltic andesite shard with typical pore structure (sample L5-4D, TVG5 Site, HHF).

9.70 wt%, MnO). The two Mn-rich crust samples have the highest Mn/Fe ratios of up to 1.11 (L5-2B) and 1.08 (L6-2B), respectively. Overall, Mn/Fe ratios are higher (0.06–1.11, mean 0.42, $n = 7$) in the samples of the HHF than those of the MHF (0.009–0.44, mean 0.11, $n = 5$).

The concentration distribution of trace elements is shown in Table 2. The crust samples of the HHF have significantly higher trace element contents (such as Li, Co, Ni, Zn, Sr and Mo) compared to those of the MHF. The concentration of (Co + Ni + Cu + Zn) of all the samples falls into the range of 97 to 727 ppm (this is also the range in the HHF), which is distinctly lower than the metalliferous sediments formed by mass wasting and corrosion of sulfides (Hrischeva et al., 2007) or hydrogenous Fe-Mn crusts (Moorby et al., 1984; Hein et al., 1997). The elements Pb and Ba in the MHF (mean 52.6 ppm and 407 ppm, respectively) are slightly enriched compared to those in the HHF (mean 7.6 ppm and 330 ppm, respectively). For example, samples L5-2B and L5-1

contain significantly high Ba concentrations (749 ppm and 365 ppm, respectively). The concentration of U appears to be uniform in the two hydrothermal fields except that the nontronite (L9-2P) contains the highest U (35.3 ppm). Overall, the distribution of trace elements from samples in the HHF is more discrete compared with that of samples from the MHF.

The hydrothermal vs. detrital contribution in sediments can be estimated using the Fe/Ti vs. $\text{Al}/(\text{Al} + \text{Fe} + \text{Mn})$ ratio (Boström, 1973). Boström (1973) showed that the ratio $\text{Al}/(\text{Al} + \text{Fe} + \text{Mn})$ is generally above 0.4 in pelagic deep-sea sediments and that lower values imply enrichment in metals. As shown in the analytical results of Table 2, all samples have the ratios of $\text{Al}/(\text{Al} + \text{Fe} + \text{Mn}) < 0.4$, indicating the minor terrigenous contribution to these deposits. In the classification scheme developed by Cox et al. (1979), the volcanic shard sample (L5-4D) falls into the category of basaltic andesite, consistent with the actual geological conditions in the VFR (Fouquet et al., 1993).

Table 2
Chemical compositions (ICP-AES and ICP-MS) of Fe–Si–Mn oxide deposits in the VFR.

Hydrothermal field	Sample	LOI ^b (wt%)	SiO ₂	Al ₂ O ₃	CaO	Fe ₂ O ₃	K ₂ O	MgO	MnO	Na ₂ O	P ₂ O ₅	TiO ₂	Total	Al/ (Al + Fe + Mn)	Mn/Fe	Li (ppm)	Sc	Cr	Co	Ni	Cu	Zn	Rb	Sr	Y	Zr	La
Hine Hina	L5-1	22.2	37.4	0.63	0.88	24.9	0.63	0.79	8.25	2.78	1.35	0.06	99.8	0.014	0.37	2.2	2.2	2.2	37.8	8.2	143	45.1	10.6	208	17.4	4.7	3.08
Hine Hina	L5-2B	20.4	52.8	0.16	1.08	9.6	0.77	0.72	9.70	4.21	0.38	0.02	99.8	0.006	1.11	1.9	2.4	4.1	29.2	15.7	98	71.3	14.3	154	10.6	2.2	2.17
Hine Hina	L5-2Y	22.6	35.9	1.15	1.15	30.9	0.34	0.7	2.38	2.59	2.09	0.11	99.9	0.025	0.09	2.0	4.1	9.0	11.7	6.0	52	27.2	6.7	172	26.0	7.2	3.77
Hine Hina	L5-3	24.6	38.5	1.49	1.3	26.7	0.31	1.15	0.64	3.45	1.58	0.15	100.0	0.040	0.03	2.8	5.2	2.8	11.7	5.9	62	46.2	8.2	132	49.0	8.4	6.16
Hine Hina	L5-4D	1.6	55.3	13.9	7.44	13.0	0.31	3.52	0.27	2.94	0.28	1.44	99.9	–	–	7.5	35	8.2	37.6	16.3	106	139.6	7.4	191	31.7	72.4	4.39
Hine Hina	L6-1	20.0	36.8	2.7	2.09	27.5	0.29	1.07	5.24	2.90	1.07	0.27	99.9	0.058	0.21	89.1	7.2	6.2	22.4	25.7	143	91.7	4.6	295	14.8	16.5	2.38
Hine Hina	L6-2B	12.6	50.5	6.11	3.95	9.5	0.47	2.25	9.29	4.25	0.27	0.61	99.7	0.189	1.08	297	16.1	7.7	46.1	66.7	443	171.8	6.9	261	17.6	32.7	3.38
Hine Hina	L6-2Y	10.9	46.2	8.9	4.79	20.4	0.35	2.46	1.06	3.00	1.02	0.90	99.9	0.238	0.06	6.8	20.7	19.9	21.3	10.0	74	85.1	6.9	216	24.5	45.2	3.93
Mariner	L9-1	16.5	61.8	0.04	0.47	14.2	0.25	0.66	0.2	5.45	0.36	0.01	99.9	0.002	0.02	2.5	1.9	3.6	0.6	3.5	169	40.0	3.4	82	0.9	1.9	0.17
Mariner	L9-2P	19.9	38.3	0.02	0.45	34.2	0.27	0.65	2.06	2.89	1.19	0.003	99.9	0.000	0.07	2.0	1.1	5.3	2.5	7.6	75	45.3	4.8	147	5.3	0.6	0.52
Mariner	L9-2Y	9.2	77.4	0.02	0.23	10.0	0.06	0.25	0.06	2.35	0.44	0.003	99.9	0.002	0.01	0.6	0.3	3.8	0.4	3.4	214	53.0	1.5	43	0.8	0.5	0.13
Mariner	L9-2G	13.7	69.9	0.03	0.34	11.4	0.19	0.58	0.09	3.37	0.29	0.004	99.9	0.002	0.01	1.5	1.9	2.5	0.7	6.2	191	92.9	4.7	64	2.2	0.9	0.29
Mariner	L9-3	16.1	56.5	0.02	0.31	17.2	0.38	0.34	6.8	2.01	0.3	0.003	99.9	0.001	0.44	0.9	0.5	2.8	20.7	20.7	65	75.2	5.0	85	1.7	0.7	0.25
Ce	Pr	Nd	Sm	Eu	Gd	Tb	Dy	Ho	Er	Tm	Yb	Lu	ΣREE	Ce/Ce*	Eu/Eu*	La _N /Lu _N	Nb	Mo	In	Cs	Ba	Hf	Ta	Tl	Pb	Th	U
6.1	0.66	3.5	0.8	0.48	1.9	0.26	1.84	0.45	1.33	0.17	0.98	0.18	21.7	0.98	1.14	1.78	0.08	365	0.05	0.37	879	0.17	0.03	1.78	8.7	0.04	12.7
5.6	0.57	2.9	0.62	0.39	1.68	0.23	1.6	0.39	1.13	0.15	0.86	0.15	18.4	1.18	1.1	1.50	0.05	749	0.05	0.35	645	0.05	0.06	2.65	4.7	0.03	17.4
10.7	1.42	7.5	2.13	0.86	4.34	0.67	4.39	1.01	2.92	0.39	2.44	0.39	43.0	1.09	0.85	1.00	0.2	96	0.05	0.44	193	0.30	0.11	0.5	5.1	0.1	11.5
13.8	1.84	9.4	2.57	1.03	5.63	0.88	6.02	1.48	4.37	0.56	3.48	0.61	57.8	0.88	0.8	1.05	0.16	27	0.05	1.04	101	0.34	0.08	0.27	20.2	0.14	22.1
12.3	1.98	11.0	3.75	1.34	4.89	0.89	5.96	1.32	3.85	0.58	3.8	0.56	56.6	0.96	0.96	0.81	1.14	2	0.12	0.22	115	2.87	0.19	0.07	1.3	0.44	0.6
3.9	0.71	3.9	1.26	0.46	1.77	0.30	2.06	0.45	1.39	0.20	1.31	0.20	20.3	0.70	0.94	1.24	0.25	175	0.16	0.26	198	0.61	0.06	2.19	7.2	0.12	2.7
5.6	1.06	5.7	1.86	0.72	2.5	0.43	3.00	0.68	2.01	0.29	1.91	0.29	29.4	0.70	1.03	1.20	0.49	920	0.11	0.2	342	1.32	0.13	5.65	6.0	0.23	2.0
9.0	1.59	8.7	2.81	1.05	3.93	0.69	4.61	0.99	2.99	0.42	2.84	0.42	43.9	0.86	0.97	0.97	0.64	38	0.14	0.41	169	1.83	0.13	0.17	7.3	0.36	1.7
0.3	0.04	0.2	0.07	0.1	0.11	0.01	0.09	0.01	0.05	0.01	0.04	0.01	1.3	0.96	3.29	1.66	0.05	28	0.16	0.14	297	0.04	0.05	0.78	37.5	0.03	3.4
1.5	0.21	1.2	0.42	0.32	0.6	0.09	0.65	0.14	0.4	0.05	0.32	0.06	6.4	1.04	1.95	0.90	0.04	89	0.19	0.41	756	0.01	0.04	7.3	94.7	0.04	35.3
0.3	0.04	0.2	0.06	0.08	0.09	0.01	0.08	0.02	0.05	0.01	0.04	0.01	1.1	0.95	3.32	1.35	0.05	38	0.22	0.10	219	0.02	0.00	0.39	35.4	0.03	2.9
0.7	0.11	0.6	0.22	0.15	0.31	0.06	0.4	0.09	0.27	0.05	0.3	0.04	3.6	0.82	1.76	0.75	0.07	21	0.24	0.38	322	0.04	0.02	0.51	62.3	0.14	2.6
0.6	0.08	0.4	0.1	0.15	0.19	0.02	0.16	0.04	0.12	0.02	0.1	0.01	2.3	1.27	3.41	2.39	0.04	165	0.07	0.14	442	0.02	0.03	14.9	33.1	0.04	5.3

^a Ce/Ce* = 2Ce_N/ (La_N + Pr_N); Eu/Eu* = 2Eu_N/ (Sm_N + Gd_N).

^b LOI-loss on ignition, at 700 °C for 2 h.

4.2.2. The patterns of rare earth element (REE)

The chondrite-normalized REE patterns of all samples are shown in Fig. 5. Generally, the REE patterns have slightly flat trends ($\text{La}_N/\text{Lu}_N = 0.75\text{--}2.39$), but there are obvious differences between the samples in the two fields. All samples of the HHF have relatively higher ΣREE concentrations (18.4–56.6 ppm, mean 36.4 ppm) with the chondrite-normalized REE pattern very similar to the basaltic andesite pattern (for example, sample L5-4D). In addition, all samples from the HHF lack positive Eu anomalies, whereas some samples show slight Ce anomalies. For instance, samples of TVG6 site all have negative Ce anomalies ($\text{Ce}/\text{Ce}^* = 0.70\text{--}0.82$, see Table 2) indicative of the contribution of seawater. The samples of the MHF have extremely low ΣREE concentrations (1.1–6.4 ppm, mean 2.9 ppm), and the chondrite-normalized REE pattern exhibits a strong positive Eu anomaly ($\text{Eu}/\text{Eu}^* = 1.76\text{--}3.41$), with no obvious Ce anomaly. This pattern from the MHF is very similar to that of a metal sulfide sample (sample L8-1, sampled during the same research cruise, Vai Lili field, unpublished data), suggestive of pronounced hydrothermal signals with negligible seawater influence.

4.3. Isotopic characteristics

4.3.1. Sr and Nd isotopes

The $^{87}\text{Sr}/^{86}\text{Sr}$ isotopic ratios of all samples are presented in Table 3, showing that most samples have relatively homogeneous isotopic contents (ranging from 0.707375 to 0.708496). Only two

samples have lower Sr isotopic ratios: one is L5-4D (0.703568), representing the composition of volcanic fragments, and the other is L6-2Y (0.706011), which is the lowest Sr isotopic value of all of the hydrothermal deposits. Samples in the HHF exhibit a more scattered trend contrasting with samples in the MHF. The Sr isotopic ratios of the HHF range from 0.706011 to 0.708496 (mean 0.707577, $n = 5$, L5-4D excluded), while those of the MHF range from 0.707748 to 0.707933 (mean 0.707836, $n = 4$). The $^{143}\text{Nd}/^{144}\text{Nd}$ isotopic ratios and ϵNd values of the two fields are reported in Table 3. All the ϵNd values are positive. Moreover, 3 samples from the HHF (sample L5-2Y, L5-3 and L5-4D) have $\epsilon\text{Nd} > 7$, whereas the crust samples (L5-2B and L6-2B) have slightly lower ϵNd values (6.67 and 5.85, respectively). The samples of the MHF have relatively high and uniform ϵNd values, ranging from 6.13 to 6.77, except that the nontronite sample (L9-2P) which has the lowest ϵNd value (0.23) of all.

4.3.2. Pb isotopes

As shown in Table 4, the $^{206}\text{Pb}/^{204}\text{Pb}$ isotopic ratios fall in the range of 18.429–18.608. The values of the samples in HHF are relatively lower and more scattered (18.429–18.598). By comparison, the values of the samples in the MHF are higher and more homogenous (18.606–18.608). The $^{207}\text{Pb}/^{204}\text{Pb}$ ratios are more uniform, and with one sample from the HHF having a low ratio (15.484, L5-2B). For the $^{208}\text{Pb}/^{204}\text{Pb}$ ratios, there are discriminating differences between the two fields: the samples from the HHF are

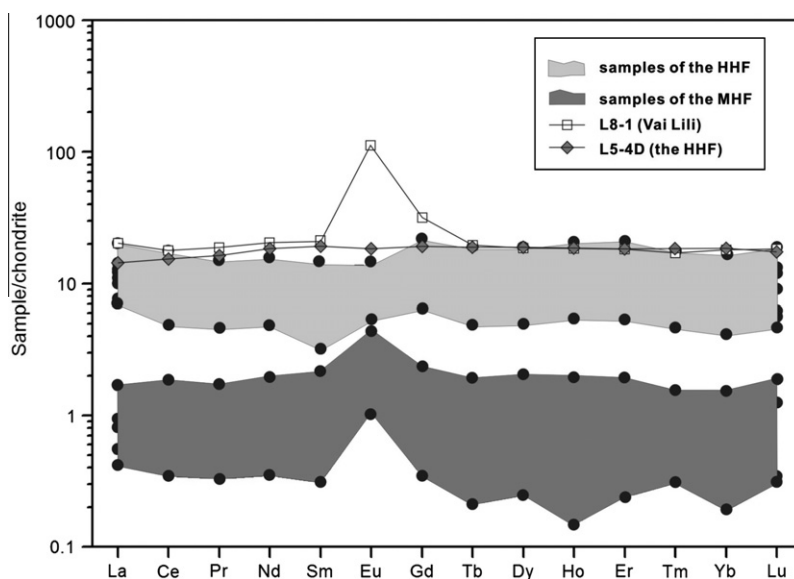


Fig. 5. Chondrite-normalized (Sun and McDonough, 1989) REE distribution patterns of the deposits from the light black area = samples from the HHF ($n = 7$); deep black area = samples from the MHF ($n = 5$); the diamond represents the basaltic andesite of this region, and the square represents the metal sulfide of this area (sample L8-1, Vai Lili hydrothermal field, unpublished data).

Table 3

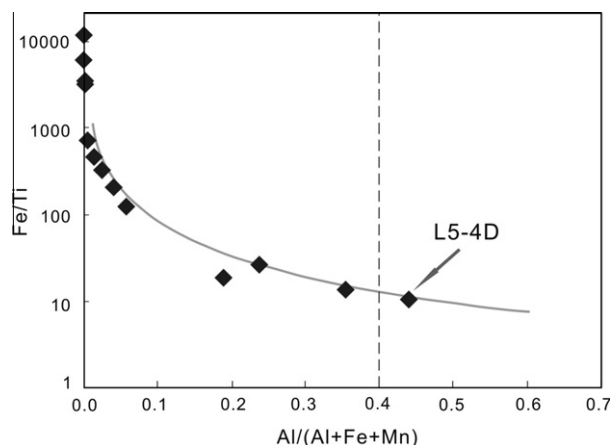
Sr–Nd isotopic compositions of the Fe–Si–Mn oxide deposits and the basaltic andesite in the VFR.

Hydrothermal field	Sample	$^{87}\text{Sr}/^{86}\text{Sr}$	$2\sigma (\times 10^6)$	$^{143}\text{Nd}/^{144}\text{Nd}$	$2\sigma (\times 10^6)$	ϵNd^*
Hine Hina	L5-2B	0.708496	4	0.512980	3	6.67
Hine Hina	L5-2Y	0.708153	5	0.513016	2	7.37
Hine Hina	L5-3	0.707850	5	0.513014	1	7.33
Hine Hina	L5-4D	0.703568	4	0.513034	5	7.72
Hine Hina	L6-2B	0.707375	5	0.512938	3	5.85
Hine Hina	L6-2Y	0.706011	3	0.512979	3	6.65
Mariner	L9-1	0.707748	3	0.512954	8	6.16
Mariner	L9-2P	0.707795	10	0.512650	5	0.23
Mariner	L9-2Y	0.707933	4	0.512986	6	6.79
Mariner	L9-2G	0.707868	4	0.512952	4	6.13

Table 4

Pb isotopic compositions of the Fe–Si–Mn oxide deposits in the VFR.

Hydrothermal field	Sample	$^{206}\text{Pb}/^{204}\text{Pb}$	$2\sigma (\times 10^3)$	$^{207}\text{Pb}/^{204}\text{Pb}$	$2\sigma (\times 10^3)$	$^{208}\text{Pb}/^{204}\text{Pb}$	$2\sigma (\times 10^3)$
Hine Hina	L5-2B	18.431	4	15.484	4	37.997	8
Hine Hina	L5-2Y	18.429	2	15.469	2	38.006	4
Hine Hina	L6-2B	18.585	1	15.469	1	38.056	3
Hine Hina	L6-2Y	18.598	1	15.469	1	38.066	2
Mariner	L9-1	18.608	1	15.463	1	38.062	2
Mariner	L9-2P	18.604	1	15.461	1	38.052	3
Mariner	L9-2Y	18.606	1	15.460	1	38.051	2
Mariner	L9-2G	18.608	1	15.461	1	38.054	2

**Fig. 6.** Plot of Fe/Ti vs. Al/(Al + Fe + Mn) for Fe–Si–Mn deposits. The sample with Al/(Al + Fe + Mn) > 0.40 is L5-4D (basaltic andesite shards) and the black line is the theoretical curve (adapted from Boström (1973)).

more scattered, ranging from 37.997 to 38.066, whereas the samples from the MHF are more homogenous ranging from 38.051 to 38.062. The overall trend of $^{208}\text{Pb}/^{204}\text{Pb}$ is in good agreement with that of $^{206}\text{Pb}/^{204}\text{Pb}$.

5. Discussion

5.1. Source origin and formation of Fe–Si–Mn oxide deposits

Contamination with terrigenous sediments, biologic detritus or mass wasting of sulfides in the sediments of the VFR are negligible, for reasons described as follow: (1) Analyses of mineralogy indicate that there are no signs of terrigenous matter incorporated in these sediments. The nontronite (the only silicate) found in the Fe–Si–Mn deposit has been demonstrated to be precipitated from hydrothermal fluids (Sun et al., in preparation). (2) Minor biological substances or pelagic oozes were observed to be mixed into the deposits. In more than 200 examinations by SEM, only one tiny relic of a diatom was found during the studies. (3) All samples have Al/(Al + Fe + Mn) values below 0.4 and fall along the theoretical curve (Fig. 6), displaying a dominant hydrothermal component with enrichments in Fe and Mn (Boström, 1973). (4) Barite, gypsum, anhydrite and metal sulfides were not recognized. The concentrations of trace metals (Cu, Zn, Co, Ni, etc.) are relatively low,

whereas the Si contents are relatively high compared to metalliferous sediment formed by mass wasting or erosion of sulfide chimneys (German et al., 1993, 1999; Hrischeva et al., 2007).

All samples exhibit perfect correlations in the plot of Al vs. Ti ($R^2 = 0.9996$) and the regression line has a zero intercept, suggesting that the Al and Ti come from the same single source (Barrett, 1992; Binns et al., 1993; Kato et al., 2005). Generally, silicate minerals are regarded as the most probable sources of Al in hydrothermal sediments (Varnavas, 1988; Gurvich, 2006). According to the chemical analyses, however, the only silicate (nontronite) contains both the lowest Al content (0.011 wt% Al_2O_3) and the lowest Al/Fe ratio (0.0004) indicating that it is impossible for silicate minerals to provide an abundant Al source. It has been argued above that the deposits lack biological debris and terrigenous matter, the most significant Al source, therefore, is the basaltic andesite fragments. As the seawater and hydrothermal fluids are both depleted in Al (Hydes, 1979; German and von Damm, 2004), the fluid can be regarded as one endmember (presumably with an Al content of zero) and the basaltic andesite (L5-4D) as the other endmember (with an Al content of 13.9 wt%). Thus the concentrations of volcanic materials mixed in the deposits were obtained through calculations. The result (Table 5) shows that the volcanic material concentrations fall into the range of 0.14–64.3 wt%. Furthermore, there is a pronounced difference between the two hydrothermal fields: the Fe–Mn oxide crusts of the HHF contain concentrations of 1.14–64.3 wt% (mean 21.8 wt%), whereas Si-rich deposits of the MHF contain concentrations of 0.14–0.27 wt% (mean 0.19 wt%). The result marks distinct different source components between the two hydrothermal fields: the Fe–Mn oxide crusts in the HHF contain a high proportion of volcanic fragments, whereas the deposits in the MHF contain minor volcanic materials if any. This result is further supported by the REE distributions of samples that show similarity to the volcanic fragments in the HHF.

Other than Al, the major geochemical difference between the two hydrothermal fields is the abundances of Si and Mn, which conforms to the deposits mineralogical characteristics in the two hydrothermal fields. In the HHF, the crust samples commonly have a laminated texture between the Fe-rich and the Mn-rich layers, in accordance with the variant Mn/Fe ratios (ranging from 0.03 to 1.11) of the subsample. According to Hein et al. (2008), these close inter laminations of Fe and Mn oxides reflect the multiple episodes of ascending hydrothermal flow. These episodes are inevitably accompanied by waning and waxing pulses of hydrothermal fluids and these pulses probably had different ratios of source components and probably differing temperature, Eh, and pH as evidenced

Table 5The calculation results of the volcanic shard concentrations in the Fe–Si–Mn oxide deposits in the VFR^a.

Hydrothermal field	Hine Hina						Mariner					
Sample	L5-1	L5-2B	L5-2Y	L5-3	L6-1	L6-2B	L6-2Y	L9-1	L9-2P	L9-2Y	L9-2G	L9-3
Basalt shards (wt%)	4.52	1.14	8.28	10.80	19.53	44.14	64.31	0.27	0.14	0.16	0.23	0.16

^a The Al concentration of L5-4D is regarded as an end member and 100% is assumed for the volcanic shard content of this sample.

by the chemical variations in the samples. A previous expedition has revealed that the Mn-rich crusts were related to pervasive diffuse discharge (10–15 °C) in the hydrothermal field of the VFR (Fouquet et al., 1993). Whereas, the Fe-rich deposits formed by diffuse flow often having slightly higher temperature, such as ~77 °C in the Eolo Seamount (Dekov et al., 2009).

Therefore, the occurrence of Mn-rich layers marks a substantially more oxygenated environment (Hein et al., 2008; Dekov et al., 2009), where the Fe and Mn exhibit a strong fractionation from parent hydrothermal fluids. Samples L5-2B and L6-2B containing higher Mn contents have relatively more abundant manganophile elements (Co, Ni, Cu, Zn) compared to the other samples. The major source of these elements is, therefore, likely to be seawater, and their concentration in the deposits will be partly a function of the degree of mixing of hydrothermal solutions with seawater and accumulation rate, which will determine how much time is available for scavenging of trace metals by the Mn oxides (Moorby et al., 1984). This hypothesis is confirmed by the negative Ce anomalies in some Mn-rich samples. However, this does not mean that the hydrogenetic contribution overwhelmingly dominates the formation of the Mn crust. The reasons are presented below: (i) the absolute contents of the manganophile elements are still much lower in these crust samples compared to those in the hydrogenetic Mn crusts. For instance, the (Co + Ni + Cu + Zn) content may reach 14,280 ppm (Moorby et al., 1984) or even higher (Hein et al., 1997) in hydrogenetic Mn crust, whereas the present Mn-rich samples only have a content of between 97 and 727 ppm, still showing strong hydrothermal characteristic. (ii) The Mn-rich crust also contains significantly higher Li (as high as 296 ppm for L6-2B), Mo (as high as 920 ppm for L6-2B and 749 ppm for L5-2B), which are always considered as indicators of a hydrothermal origin (Moorby et al., 1984; Chan and Hein, 2007).

The growth rates of Mn mineralization can provide further good constraints for the source and origin of the Fe–Mn oxide crusts. Selecting four Mn-rich samples from the HHF, the growth rate was calculated using the empirical equation developed by Manheim and Lane-Bostwick (1988): growth rate $R = 0.68 / (Co^n)^{1.67}$, where the normalized Co is $Co^n = Co \times 50 / (Fe + Mn)$, and Co, Fe and Mn are measured concentrations in weight percent. The result (see Table 6) shows that the growth rate ranges from 634 to 5027 mm Ma⁻¹, which is significantly higher than the growth rates of hydrogenetic Mn crusts (0.15–15 mm Ma⁻¹; Hein et al., 1997). Nevertheless, the two Mn-rich samples (L5-2B and L6-2B) have lower growth rates adjacent to the lower limit of the hydrothermal Mn crust (1000 to 100,000 mm Ma⁻¹; Hein et al., 1997), manifesting some contributions of the ambient seawater.

In the MHF, the presence of positive Eu anomalies, absence of negative Ce anomalies and the depletion in ΣREE indicate that seawater has made few contribution to the deposit, in other words, the hydrothermal Si-rich deposits experienced relatively rapid precipitation in the area. The general geochemical Pb anomalies along with Cu in some samples of the MHF (as high as 94.7 and 214 ppm, respectively) predominantly reflect the close proximity to the hydrothermal jet or sulfide precipitates at depth, indicating greater hydrothermal fluid supply. The high Ba content (297–756 ppm) is probably attributable to disseminated barite aggregates. Finely, dispersed hydrothermal barite is found throughout the bottom

waters of the Lau Basin (Marchig et al., 1992, adapted from Daesslé and Cronan, 2002). Thus, a hydrothermal source for Ba in the Si-rich deposits is likely. The presence of barite has not been confirmed, possibly due to the poor XRD detection limit (generally $\pm 5\%$). It is worth emphasizing that the Mn-rich deposits in the HHF also contain relatively high Ba (up to 879 ppm for sample L5-1, for instance). Besides a barite contribution, Ba-rich todokorite and basaltic andesite fragments may be expected to provide other sources.

At the same time, the high accumulation of opal-A in the MHF reveals the occurrence of conductive cooling of the hydrothermal fluids. As previous studies have shown, the simple mixing of hydrothermal fluid with seawater does not evoke the precipitation of Si in modern hydrothermal systems (Herzig et al., 1988; Stüben et al., 1994). The large-scale occurrence of opal-A thus represents a sluggish mixing between hydrothermal fluid and seawater. One possible interpretation is a deep location of the magma reservoir underlying the CVFR (e.g., 3.2 km) relative to those found along the mid-ocean ridges (e.g., 1.2–2.4 km beneath the East Pacific Rise; Detrick et al., 1987). The deeper location results in a longer ascent time for hydrothermal fluid than the ascent time found in mid-ocean ridges, and consequently leads to conductive cooling. The other reason maybe relates to the ubiquitous biogenetic Fe oxide filaments in the deposits. A porous, filamentous structure formed by the neutrophilic Fe-oxidizing bacteria, partly filled by Fe oxides could limit the mixing between hydrothermal water and seawater. The consequent conductive cooling could permit silica saturation and evoke the precipitation of opal-A (Juniper and Fouquet, 1988).

5.2. Factors affecting $^{87}Sr/^{86}Sr$ and $^{143}Nd/^{144}Nd$ ratios

The $^{87}Sr/^{86}Sr$ ratios of all samples fall into a range, which is less than seawater and higher than substrate rock (Fig. 7A), suggesting the absence of obvious radiogenic Sr source. Overall, there are two clusters of samples in Fig. 7A showing two trends of the $^{87}Sr/^{86}Sr$ ratios. The approximately linear cluster of the MHF samples (~ 0.7080) shows that the Sr concentration has a minimal influence on the $^{87}Sr/^{86}Sr$ ratio, indicating sufficient hydrothermal fluid supplies from which the minerals precipitate. The samples of the HHF, however, show a strikingly contrasting cluster with relatively stable contents but systematic variations in $^{87}Sr/^{86}Sr$ ratios ranging from 0.7036 to 0.7085. One possible factor is the effect of volcanic materials. Alternatively, the sample containing the least amount of volcanic fragments (i.e. the samples of TVG5, excluding L5-4D) has the highest $^{87}Sr/^{86}Sr$ ratio indicating that the seawater contributes significant portions of Sr to the hydrothermal deposits. Generally, seawater is not obviously depleted in Sr compared to the hydrothermal fluids in the Lau Basin (88 μm and 93–199 μm , respectively; Mottl et al., 2011). A small seawater addition will lead to appreciable fluctuation of the Sr isotopes. Thus, in the HHF, the $^{87}Sr/^{86}Sr$ ratio of the hydrothermal deposits represents a mixture of three components, namely hydrothermal fluids, seawater and volcanic materials, whereas in the MHF, this ratio is mainly controlled by hydrothermal fluids.

The mass difference between the two Sr isotopes, ^{87}Sr and ^{86}Sr , is too small to cause a measurable fractionation during precipitation, therefore, the $^{87}Sr/^{86}Sr$ ratio in hydrothermal minerals can be used as a direct measure of its ratio in the parent fluid (Pichler and Veizer, 1999, 2004). For the MHF, assuming no conductive loss or gain of heat and using the average temperatures of bottom seawater and hydrothermal fluid in this area (2 °C and 299.4 °C, respectively; Mottl et al., 2011), the temperature of the mixture can be calculated with the mass balance equation:

$$T_M = (1 - y)t_{HF} + yt_{SW} \quad (1)$$

Table 6
The calculated growth rates of Mn-rich oxide crusts in the HHF.

Sample	Fe (wt%)	Mn (wt%)	Co (wt%)	GR (mm Ma ⁻¹)
L5-1	17.39	6.39	0.0037840	2179
L5-2B	6.74	7.51	0.0029180	1431
L6-1	19.24	4.06	0.0022370	5067
L6-2B	6.64	7.19	0.0046120	634

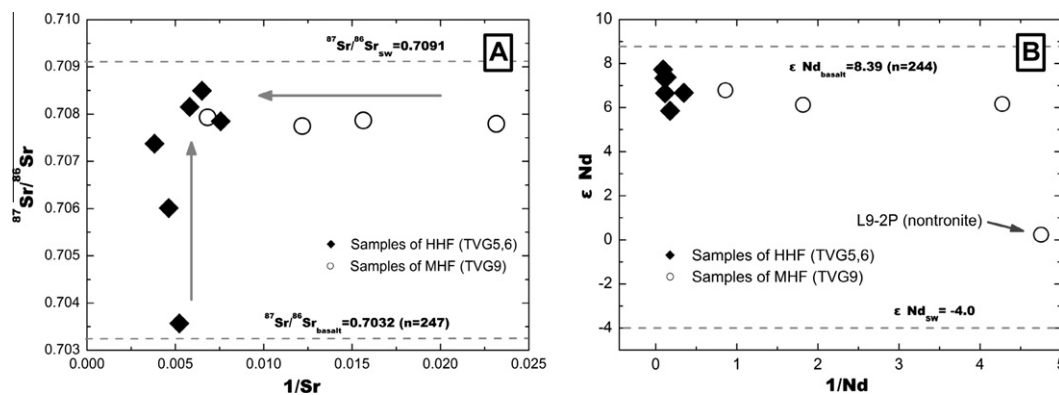


Fig. 7. Plots of $^{87}\text{Sr}/^{86}\text{Sr}$ ratios vs. $1/\text{Sr}$ (A) and ϵNd values vs. $1/\text{Nd}$ (B). The dashed line in the upper part of figure A represents the Sr isotope ratio of modern seawater (SW), 0.7091 (Mottl et al., 2011) and the dashed line in the lower part represents the Sr isotope ratio of substrate rock in the VFR region ($n = 247$). The dashed line in the upper part of figure B represents the ϵNd values of substrate rock in the VFR region ($n = 247$), and the dashed line in the lower part represents the Nd value of the lower limit of ϵNd of modern Pacific deep water (Goldstein and Hemming, 2003). All the Sr and Nd isotope data for the substrate rock in this area come from the GEOROC database (<http://georoc.mpch-mainz.gwdg.de/georoc/>).

where t_M is the temperature of the mixture, t_{HF} is the temperature of the hydrothermal fluid, t_{SW} is the temperature of seawater, and y is the seawater fraction. For the hydrothermal endmember and the bottom seawater in the MHF, the average $^{86}\text{Sr}/^{87}\text{Sr}$ ratios of 0.7042 and 0.7091 (Mottl et al., 2011) are adopted. The calculated minimum and maximum seawater fractions are approximately 72.8% and 76.6%, respectively. Thus, the precipitation of the MHF hydrothermal sediment takes place within a relatively narrow temperature range between 72 and 83 °C, indicating the relatively stable characteristics of the hydrothermal activity, verifying the higher precipitation temperature in the MHF.

All the samples (excluding the nontronite sample L9-2P) have significantly higher ϵNd values than seawater and approach the substrate rock values in this region (as shown in Fig. 7B). Similarly to the Sr isotopes, the ϵNd trend of the samples of the HHF is slightly shifted towards seawater. This observation hints at the contributions by seawater and verifies the $^{87}\text{Sr}/^{86}\text{Sr}$ implication. The shift of the ϵNd trend is not obvious probably because of the relatively minor Nd concentrations in seawater (only 0.03 $\mu\text{g/L}$, Li, 1982) contrasting with that in the hydrothermal fluid (for instance, the Nd concentration in the EPR endmember vent fluid is 500 times higher than that of ambient seawater; Hinkley and Tatsumoto, 1987). In the MHF, all three samples (excluding the nontronite) have very uniform ϵNd values. As discussed previously, the hydrothermal source dominates the hydrothermal deposits of the MHF. Thus, the ϵNd values (6.13 to 6.79, mean 6.36) possibly reflect the Nd isotope signature of hydrothermal fluids in this area.

Even the hydrothermal deposits in the MHF (with minor influence of volcanic fragments and/or seawaters) have a distinct Nd isotope trend compared to the results of previous studies based on hydrothermal distal plume deposits (e.g., German et al., 1990; Halliday et al., 1992; van de Flierdt et al., 2004; Chavagnac et al., 2006). This may reflect the distinct behavior of Nd in these different hydrothermal flows. Prior to ascending, the diffuse flow cannot mix intensively with ambient seawater at depth due to the isolation and constraints of the preformed sediments. The Fe–Mn oxide particles only scavenge the hydrothermal Nd rather than the seawater Nd before precipitation. Consequently, the deposits formed by sufficient hydrothermal diffuse fluids essentially retain the initial hydrothermal ϵNd values with minor seawater influence. Other studies mentioned above are all based on the distal plume sediments. During the long distance dispersion, the hydrothermal fluids mix with the ambient seawater freely, hence abundant seawater Nd incorporates into the sediment, and the Nd isotope ratio is considered to reflect the ambient seawater rather than the hydrothermal fluids.

The nontronite (L9-2P) contains the most significantly anomalous Nd isotope value (which approaches that of seawater) of all samples. The most probable explanation is that the Nd isotopes in nontronite had an adequate exchange with ambient seawater. The authigenic hydrothermal nontronite is favorable for precipitation under redox conditions (Köhler et al., 1994), where hydrothermal fluids mix with seawater on a relatively large scale. Consequently, isotopic exchanges between hydrothermal fluid and seawater occur. The highest U content (marking the seawater contribution, e.g., Bender et al., 1971; Dymond et al., 1973; Mills et al., 1993) in the sample verifies this suggestion.

5.3. Pb isotopic compositions and implications

Lead isotope ratios provides powerful tools for determining the relative contribution of crustal (non-radiogenic) and pelagic (radiogenic) sources (Mills et al., 1993; German et al., 1999; van de Flierdt et al., 2004; Dias et al., 2008). As shown in the diagram of $^{206}\text{Pb}/^{204}\text{Pb}$ vs. $^{208}\text{Pb}/^{204}\text{Pb}$ (Fig. 8), the hydrothermal deposits in the VFR plot in the Pacific MORB area, somewhat distant from the pelagic sediments and the Pacific Deep Waters (PDW), hint at a trivial influence of radiogenic source on the Pb isotope system. Moreover, the Pb isotopes in the samples are less radiogenic than those of the fresh lava and sulfides in this area. At the same time, they exhibit a close association with the basalt in the central and southern Tonga island arc. All these observations imply that the Pb in the samples originates from the leaching of ancient crusts. The contributions of Pb from potential distal plumes are considered to be minor because there are no significant signatures of fresh volcanic, lava and even the northern Tonga island arc crust in this area. As a particle-reactive element (Schaule and Patterson, 1981; Cochran et al., 1990; Frank et al., 2002), Pb has a much shorter oceanic residence time of 80–100 a (Frank et al., 2002) with a trivial content in seawater (not more than 0.01 nM; Fouquet et al., 1991), which also makes it difficult for copious amounts of Pb to migrate by means of non-buoyant hydrothermal flow.

Nevertheless, in the HHF, the Pb isotope signatures of some samples still exhibit some departure from the overall trend. It is supposed that this reflects the complexity of the geological setting of the HHF located at the propagating rift tip, which is now in a volcanic stage and the hydrothermal system contains two distinct parts topographically (e.g., Fouquet et al., 1993). The deeper part is hosted by massive lava flows and has focused flow along faults, whereas the upper part is characterized by volcanoclastic materials (with estimated thicknesses of up to 50 m; Fouquet et al., 1993).

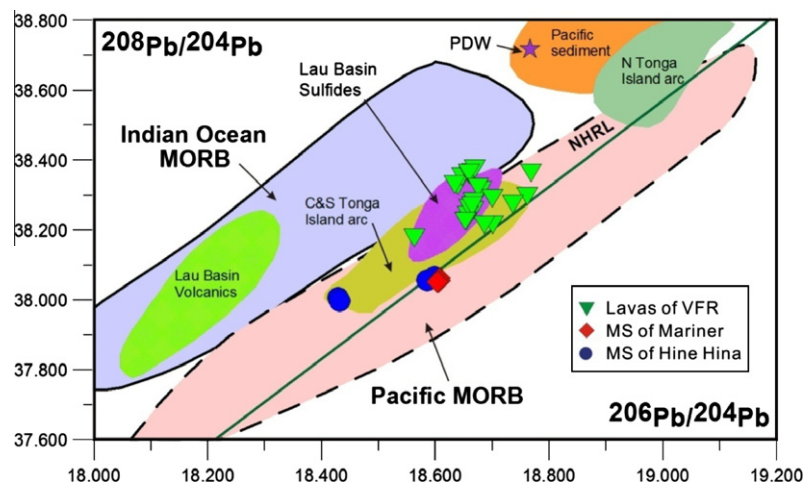


Fig. 8. Diagrams of $^{206}\text{Pb}/^{204}\text{Pb}$ vs. $^{208}\text{Pb}/^{204}\text{Pb}$ for Fe–Si–Mn oxide deposits in the VFR region; the error for the samples is less than the diameters of the symbols. The Pb isotopic composition of the PDW is from Abouchami et al., 1999 (average value of two samples); the NHRL (Northern Hemisphere Reference Line) comes from Hart, 1984; the Pb isotopes for the Lau Basin metal sulfides come from Fouquet and Marcoux (1995) and the Pb isotopes of the VFR lavas and other data of unspecified origin all come from Fretzdorff et al. (2006).

and low-temperature diffuse venting. The TVG6 site is possibly controlled by the deeper part of the hydrothermal system, resulting in the Pb isotope of deposits being closer to their counterparts of fresh lava and similar to those of the MHF. In contrast, the TVG5 site is probably located in the upper part of the hydrothermal system where the diffuse flow and the volcanic debris are pervasive. Because of extremely high solubility in hydrous fluids (Keppler, 1996), a portion of the Pb leached from volcanic debris by the hydrothermal fluids could be expected to add to the deposits. The presence of saponite further supports this viewpoint. Thus, the Pb in the sample from the TVG5 site may come from the pre-formed old volcanoclastic layer rather than the fresh lava. In all, the Pb isotopes in these deposits are ultimately controlled by the characteristics of the substrate rock or preformed volcanoclastic layers in the plumbing system. This constitutes an essential contrast to the sulfide and metalliferous sediments formed by distal plumes.

5.4. The indication of the hydrothermal diffuse flow Fe–Mn oxide crust

The Fe–Mn oxide crusts were observed along the crest of the southern VFR at a distance of about 4 km, representing the first stage of hydrothermal activity of broad diffuse flow through permeable vesicular and brecciated basaltic andesites (Fouquet et al., 1993). Compared to the spreading history of the Lau Basin, the Mn-rich layers occur intermittently throughout the entire evolution of the basin. Previous studies based on metalliferous sediment drill cores from the Lau Basin have shown that the maximum Mn accumulation rates occurred at 3.2 Ma and 1.0 Ma. The Mn/Fe ratios of 0.76–0.92 and 0.48–0.50 exactly coincide with the climaxes of the propagating activities of the ELSC and the VFR, respectively (Cronan and Hodkinson, 1997). Furthermore, the studies concentrated on the somewhat younger (0–30 ka) hydrothermal sediments of the VFR also defined a characteristic Mn/Fe ratio ranging from 0.36 to 0.83 ($n = 8$, originally presented as Fe/Mn; Daesslé et al., 2000). In the present research, however, the two Fe–Mn oxide crust samples of the HHF contain Mn/Fe ratios slightly higher than those discussed above. This may reflect the present, fairly intensive, southward propagating rifting in the SVFR. Notwithstanding the fact that the Mn/Fe ratios of the samples are higher than those found in the previous studies, a point worth emphasizing is that the other studies are based on distal plume precipitates, while the present samples represent the diffuse flow

deposits in hydrothermal fields. This means that the actual intensities of spreading activity cannot be equated with each other because of the differences of fractionation between Fe and Mn in different environments. However, the higher Mn/Fe ratio of the present samples still provides an indicator of the propagating activity of the VFR, like that at 3.2 Ma and 1.0 Ma.

For the MHF in CVFR, all samples have much lower Mn/Fe ratios than those found in the HHF (all samples falling within the range of 0.067–0.007, except for one sample at 0.43). This suggests that the fluids of the MHF are now in a more stable state. This result is consistent with those of previous studies (Fouquet et al., 1993).

6. Conclusions

The absence of pelagic oozes, terrigenous matter and metal sulfide debris indicates that the Fe–Si–Mn oxide deposits in the HHF and the MHF are predominately formed by hydrothermal diffuse flow. In the HHF, the Fe–Mn oxide crusts are mainly composed of birnessite, todokorite and HFO, along with variable amounts of volcanic fragments. Whereas in the MHF, opal-A and patchy nontonite are the predominate constituents with few volcanic materials. The occurrence of Fe–Mn oxide crusts is indicative of a more oxygenated environment with seawater influence, whereas the large-scale opal-A indicates conductive cooling of hydrothermal fluids.

The hydrothermal deposits in the HHF are enriched in Fe, Mn and Al, whereas in the MHF contain higher concentrations of Si. Some levels of trace elements (Co, Ni, Zn, Sr, and Mo) and ΣREE are higher in the HHF than in the MHF, indicating the contribution of seawater. This suggestion is further supported by the Ce anomalies in the HHF. The geochemical anomalies of Pb and Ba, along with distinct positive Eu anomalies in the MHF, suggest the close affinity of a hydrothermal jet. The growth rates based on the Co content of Mn-rich deposits were determined to be between 634 and 5027 mm Ma^{−1}, which is significantly higher than those of hydrogenetic Mn crusts. The Sr, Nd and Pb isotopes provide further constraints regarding the source components and formations in Fe–Si–Mn oxide deposits from both hydrothermal fields. In the HHF, the Sr isotope distribution shows discrete trends, indicating mixing between hydrothermal fluids and ambient seawater. The Nd isotope distribution in the HHF shows an insignificant shift towards seawater, mainly because of the depletion of Nd in seawater.

Both the Sr and Nd isotopes in the MHF are relatively homogeneous, indicating a sufficient supply of hydrothermal fluids in this area. The surprising result is that the Nd isotope signal in the diffuse flow generally reflects an origin of hydrothermal fluids. This result is quite different from the metalliferous sediments formed by distal plumes. The remarkable departure of the Pb isotopes from the pelagic sediments and PDW indicates that the Pb source in Fe–Si–Mn oxide deposits is ultimately controlled by both hydrothermal fluid and basement rock or preformed sediments.

This study suggests that the high concentrations of Mn in the hydrothermal fluids (5800–7100 $\mu\text{mol/kg}$) and the relatively lower Fe concentration (1200–2900 $\mu\text{mol/kg}$) account for the formation of Fe–Mn oxide crusts in the HHF. The Mn/Fe ratio of hydrothermal deposits formed by diffuse flow may be a good indicator of propagating activities in the VFR, such as the activities at 3.2 and 1.0 Ma.

Acknowledgements

This study was supported by the Natural Science Foundation of China (Project Nos. 40976045, 40976025 and 40976036). We thank Professor Fuya Wang from the Guangzhou Institute of Geochemistry, Chinese Academy of Sciences, for his analytical help with XRD. We also thank two anonymous reviewers for their valuable comments and constructive suggestions.

References

- Abouchami, W., Galer, S.J.G., Koschinsky, A., 1999. Pb and Nd isotopes in NE Atlantic Fe–Mn crusts: Proxies for trace metal paleosources and paleocean circulation. *Geochim. Cosmochim. Acta* 63, 1489–1505.
- Alt, J.C., 1988. The chemistry and sulfur isotope composition of massive sulfide and associated deposits on Green Seamount, Eastern Pacific. *Econ. Geol.* 83, 1026–1033.
- Barrett, T.J., 1992. Mass changes in the Galapagos hydrothermal mounds: near-axis sediment transformation and mineralization. *Geology* 20, 1075–1078.
- Bender, M., Broecker, W.S., Gornitz, V., Middel, U., Day, R., Sun, S.S., Biscaye, P., 1971. Geochemistry of three cores from the East Pacific Rise. *Earth Planet. Sci. Lett.* 12, 425–433.
- Binns, R.A., Scott, S.D., Bogdanov, Y.A., Lisitzin, A.P., Gordeev, V.V., Gurvich, E.G., Finlayson, E.J., Boyd, T., Dotter, L.E., Wheller, G.E., Mu-ravyev, K.G., 1993. Hydrothermal oxide and gold-rich sulfate deposits of Franklin Seamount, Western Woodlark Basin, Papua New Guinea. *Econ. Geol.* 88, 2122–2153.
- Boström, K., 1973. The origin and fate of ferromanganese active ridge sediments. *Stockholm Contrib. Geol.* 27, 149–243.
- Boyd, T.D., Scott, S.D., 1999. Two-XRD-line ferrihydrite and Fe–Si–Mn oxyhydroxide mineralization from Franklin Seamount, western Woodlark Basin, Papua New Guinea. *Can. Miner.* 37, 973–990.
- Chan, L.-H., Hein, J.R., 2007. Lithium contents and isotopic compositions of ferromanganese deposits from the global ocean. *Deep Sea Res., Part II* 54, 1147–1162.
- Chavagnac, V., Palmer, M.R., Milton, A., Green, D.R.H., German, C.R., 2006. Hydrothermal sediments as a potential record of seawater Nd isotope compositions: the Rainbow vent site (36°14'N, Mid-Atlantic Ridge). *Paleoceanography* 21, PA3012. doi:10.1029/2006PA001273.
- Cochran, J.K., McKibbin-Vaughan, T., Dornblaser, M.M., Hirschberg, D., Livingston, H.D., Buesseler, K.O., 1990. ^{210}Pb scavenging in the North Atlantic and North Pacific Oceans. *Earth Planet. Sci. Lett.* 97, 332–352.
- Collier, J.S., Sinha, M.C., 1990. Seismic images of a magma chamber beneath the Lau Basin back-arc spreading centre. *Nature* 346, 646–648.
- Collier, J.S., Sinha, M.C., 1992. Seismic mapping of a magma chamber beneath the Valu Fa Ridge, Lau Basin. *J. Geophys. Res.* 97, 14031–14053.
- Cornell, R.M., Schwertmann, U., 1996. The Iron Oxides: Structure, Properties, Reactions, Occurrence and Uses. VCH, Germany.
- Cox, K.G., Bell, J.D., Pankhurst, R.J., 1979. The Interpretation of Igneous Rocks. Allen and Unwin, London.
- Cronan, D.S., Hodkinson, R.A., 1997. Geochemistry of hydrothermal sediments from ODP Sites 834 and 835 in the Lau Basin, southwest Pacific. *Mar. Geol.* 141, 237–268.
- Daesslé, L.W., Cronan, D.S., 2002. Late Quaternary hydrothermal sedimentation adjacent to the Central Lau Spreading Center. *Mar. Geol.* 182, 389–404.
- Daesslé, L.W., Cronan, D.S., Marchig, V., Wiedicke, M., 2000. Hydrothermal sedimentation adjacent to the propagating Valu Fa Ridge, Lau Basin, SW Pacific. *Mar. Geol.* 162, 479–500.
- Dekov, V., Savelli, C., 2004. Hydrothermal activity in the SE Tyrrhenian Sea: an overview of 30 years of research. *Mar. Geol.* 204, 161–185.
- Dekov, V.M., Kamenov, G.D., Savelli, C., Stummeyer, J., Thirye, M., Shanks, W.C., Willingham, A.L., Boycheva, T.B., Rochette, P., Kuzmann, E., Fortini, D., Vértés, A., 2009. Metalliferous sediments from Eolo Seamount (Tyrrhenian Sea): hydrothermal deposition and re-deposition in a zone of oxygen depletion. *Chem. Geol.* 264, 347–363.
- Dekov, V.M., Petersen, S., Garbe-Schönberg, C.-D., Kamenov, G.D., Perner, M., Kuzmann, E., Schmidt, M., 2010. Fe–Si-oxyhydroxide deposits at a slow-spreading centre with thickened oceanic crust: The Lilliput hydrothermal field (9°33'S, Mid-Atlantic Ridge). *Chem. Geol.* 278, 186–200.
- Detrick, R.S., Buhl, P., Vera, E.E., Mutter, J.C., Orcutt, J.A., Madsen, J.A., Brocher, T.M., 1987. Multi-channel seismic imaging of a crustal magma chamber along the East Pacific Rise. *Nature* 326, 35–41.
- Dias, Á.S., Mills, R.A., Taylor, R.N., Ferreira, P., Barriga, F.J.A.S., 2008. Geochemistry of a sediment push-core from the Lucky Strike hydrothermal field, Mid-Atlantic Ridge. *Chem. Geol.* 247, 339–351.
- Dymond, J., Corliss, J.B., Heath, G.R., Field, C.W., Dasch, E.J., Veeh, H.H., 1973. Origin of metalliferous sediments from the Pacific Ocean. *Geol. Soc. Am. Bull.* 84, 3355–3371.
- Emerson, D., Rentz, J.A., Lilburn, T.G., Davis, R.E., Aldrich, H., Chan, C., Moyer, C.L., 2007. A novel lineage of proteobacteria involved in formation of marine Fe-oxidizing microbial mat communities. *PLoS One* 2 (7), e667. doi:10.1371/journal.pone.0000667.
- Ferrini, V.L., Tivey, M.K., Carbotte, S.M., Martinez, F., Roman, C., 2008. Variable morphologic expression of volcanic, tectonic, and hydrothermal processes at six hydrothermal vent fields in the Lau back-arc basin. *Geochim. Geophys. Geosys.* 9, Q07022. doi:10.1029/2008GC002047.
- Fouquet, Y., Marcoux, E., 1995. Lead isotope systematics in Pacific hydrothermal sulfide deposits. *J. Geophys. Res.* 100 (B4), 6025–6040.
- Fouquet, Y., von Stackelberg, U., Charlou, J.L., Donval, J.L., Erzinger, J., Foucher, J.P., Herzig, P., Muhe, R., Soakai, S., Wiedicke, M., 1993. Metallogenesis in back-arc environments: the Lau Basin example. *Econ. Geol.* 88, 2154–2181.
- Fouquet, Y., von Stackelberg, U., Charlou, J.L., Donval, J.P., Foucher, J.P., Erzinger, J., Herzig, P., Muhe, R., Wiedicke, M., Soakai, S., Whitechurch, H., 1991. Hydrothermal activity in the Lau back-arc basin: sulfides and water chemistry. *Geology* 19, 303–306.
- Frank, M., Whiteley, N., Kasten, S., Hein, J.R., O'Nions, K., 2002. North Atlantic DeepWater export to the Southern Ocean over the past 14 Myr: evidence from Nd and Pb isotopes in ferromanganese crusts. *Paleoceanography* 17. doi:10.1029/2000PA000606.
- Fretzdorff, S., Schwarz-Schampera, U., Gibson, H.L., Garbe-Schönberg, C.-D., Hauff, F., Stoffers, P., 2006. Hydrothermal activity and magma genesis along a propagating back-arc basin: Valu Fa Ridge (Southern Lau Basin). *J. Geophys. Res.* 111, B08205. doi:10.1029/2005JB003967.
- German, C.R., von Damm, K.L., 2004. Hydrothermal processes. In: Elderfield, H. (Ed.) *The Oceans and Marine Geochemistry*, Holland, H.D., Turekian, K.K. (Exec. Eds.), Treatise on Geochemistry, vol. 6. Elsevier, pp. 181–222.
- German, C.R., Hergt, J., Palmer, M.R., Edmond, J.M., 1999. Geochemistry of a hydrothermal sediment core from the OBS vent-field, 218N East Pacific Rise. *Chem. Geol.* 15, 65–75.
- German, C.R., Higgs, N.C., Thomson, J., Mills, R.A., Elderfield, H., Blusztajn, J., Fleer, A.P., Bacon, M.P., 1993. A geochemical study of metalliferous sediment from the TAG hydrothermal mound, 26°08'N, Mid-Atlantic Ridge. *J. Geophys. Res.* 98, 9683–9692.
- German, C.R., Klinkhammer, G.P., Edmond, J.M., Mttira, A., Elderfield, H., 1990. Hydrothermal scavenging of rare-earth elements in the ocean. *Nature* 345, 516–518.
- Goldstein, S.L., Hemming, S.R., 2003. Long-lived isotopic tracers in oceanography, paleoceanography, and ice-sheet dynamics. In: Elderfield, H. (Ed.), *The Oceans and Marine Geochemistry*, Holland, H.D., Turekian, K.K. (Exec. Eds.), Treatise on Geochemistry, vol. 6. Elsevier, pp. 453–489.
- Gurvich, E.G., 2006. *Metalliferous Sediments of the World Ocean: Fundamental Theory of Deep-Sea Hydrothermal Sedimentation*. Springer-Verlag, Berlin, Heidelberg.
- Halliday, A.N., Davidson, J.P., Holden, P., Owen, R.M., Olivarez, A.M., 1992. Metalliferous sediments and the scavenging residence time of Nd near hydrothermal vents. *Geophys. Res. Lett.* 19, 761–764.
- Hannington, M.D., Galley, A.G., Herzig, P.M., Petersen, S., 1998. A comparison of the TAG Mound and stockwork complex with Cyprus-type massive sulfide deposits. *Proc. Ocean Drilling Program, Scientific Results Volume Leg 158*, 389–415.
- Hart, S.R., 1984. The Dupal anomaly: a large-scale isotope anomaly in the southern hemisphere mantle. *Nature* 309, 753–757.
- Hawkins, 1995. Evolution of the Lau Basin-insights from ODP Leg 135. In: Taylor, B., Natland, J. (Eds.), *Active Margins and Marginal Basins of the Western Pacific*. Am. Geophys. Union, 125–173.
- Hein, J.R., Koschinsky, A., Halbach, P., Manheim, F.T., Bau, M., Kang, J.-K., Lubick, N., 1997. Iron and manganese oxide mineralization in the Pacific. In: Nicholson, K., Hein, J.R., Bühn, B., Dasgupta, S. (Eds.), *Manganese Mineralization: Geochemistry and Mineralogy of Terrestrial and Marine Deposits*. Geol. Soc. Spec. Publ. vol. 119, 123–138.
- Hein, J.R., Schulz, M.S., Dunham, R.E., Stern, R.J., Bloomer, S.H., 2008. Diffuse flow hydrothermal manganese mineralization along the active Mariana and southern Izu-Bonin arc system, western Pacific. *J. Geophys. Res.* 113, B08S14. doi:10.1029/2007JB005432.
- Hekinian, R., Hoffer, M., Larque, P., Cheminee, J.-L., Stoffers, P., Bideau, D., 1993. Hydrothermal Fe and Si oxyhydroxide deposits from South Pacific intraplate volcanoes and East Pacific Rise axial and off-axial regions. *Econ. Geol.* 88, 2099–2121.

- Herzig, P.M., Becker, K.P., Stoffers, P., Bäcker, H., 1988. Hydrothermal silica chimney fields in the Galapagos Spreading Center at 86W. *Earth Planet. Sci. Lett.* 89, 261–272.
- Hinkley, T.K., Tatsumoto, M., 1987. Metal and isotopes in Juan de Fuca Ridge hydrothermal fluids and their associated solid materials. *J. Geophys. Res.* 92, 11400–11410.
- Hrischeva, E., Scott, S.D., 2007. Geochemistry and morphology of metalliferous sediments and oxyhydroxides from the Endeavour segment, Juan de Fuca Ridge. *Geochim. Cosmochim. Acta* 71, 3476–3497.
- Hrischeva, E., Scott, S.D., Weston, R., 2007. Metalliferous sediments associated with presently forming volcanogenic massive sulfides: the SuSu Knolls hydrothermal field, eastern Manus Basin, Papua New Guinea. *Econ. Geol.* 102, 55–73.
- Hydes, D.J., 1979. Aluminum in seawater – control by inorganic processes. *Science* 4412, 1260–1262.
- Iizasa, K., Kawasaki, K., Maeda, K., Matsumoto, T., Saito, N., Hirai, K., 1998. Hydrothermal sulfide-bearing Fe–Si oxyhydroxide deposits from the Coriolis Troughs, Vanuatu backarc, southwestern Pacific. *Mar. Geol.* 145, 1–21.
- Jenner, G.A., Cawood, P.A., Rautenschlein, M., White, W.M., 1987. Composition of back-arc basin volcanics, Valu Fa Ridge, Lau Basin: evidence for a slab-derived component in their mantle source. *J. Volcan. Geotherm. Res.* 32, 209–222.
- Juniper, S.K., Fouquet, Y., 1988. Filamentous iron-silica deposits from modern and ancient hydrothermal site. *Can. Miner.* 26, 859–869.
- Jones, J.B., Segnit, F.R., 1971. The nature of opal. 1. Nomenclature and consistent phases. *J. Geol. Soc.* 18, 57–68.
- Kato, S., Kobayashi, C., Kakegawa, T., Yamagishi, A., 2009. Microbial communities in iron-silica-rich microbial mats at deep-sea hydrothermal fields of the Southern Mariana Trough. *Environ. Microbiol.* 11, 2094–2111.
- Kato, Y., Fujinaga, K., Suzuki, K., 2005. Major and trace element geochemistry and Os isotopic composition of metalliferous umbers from the late Cretaceous Japanese accretionary complex. *Geochem. Geophys. Geosys.* 6, Q07004. doi:10.1029/2005GC000920.
- Kennedy, C.B., Martinez, R.E., Scott, S.D., Ferris, F.G., 2003. Surface chemistry and reactivity of bacteriogenic iron oxides from Axial Volcano, Juan de Fuca Ridge, north-east Pacific Ocean. *Geobiology* 1, 59–69.
- Keppler, H., 1996. Constraints from partitioning experiments on the composition of subduction-zone fluids. *Nature* 380, 237–240.
- Köhler, B., Singer, A., Stoffers, P., 1994. Biogenic nontronite from marine white smoker chimneys. *Clays Clay Miner.* 42, 689–701.
- Lécuyer, C., Dubois, M., Marignac, C., Gruau, G., Fouquet, Y., Ramboz, C., 1999. Phase separation and fluid mixing in subseafloor back arc hydrothermal systems: a microthermometric and oxygen isotope study of fluid inclusions in the barite-sulfide chimneys of the Lau basin. *J. Geophys. Res.* 104, 17911–17927.
- Li, Y.H., 1982. A brief discussion on the mean oceanic residence time of elements. *Geochim. Cosmochim. Acta* 46, 2671–2675.
- Little, C.T.S., Glynn, S.E.J., Mills, R.A., 2004. Four-hundred and ninety-million-year record of bacteriogenic iron oxide precipitation at sea-floor hydrothermal vents. *Geomicrobiol. J.* 21, 415–429.
- Manheim, F.T., Lane-Bostwick, C.M., 1988. Cobalt in ferromanganese crusts as a monitor of hydrothermal discharge on the Pacific seafloor. *Nature* 335, 59–62.
- Marchig, V., Wiedicke, M., Riech, V., 1992. Hydrothermal Anomaly in the Sea Water of the Lau Basin. Final Report SONNE Cruise 67-2, Bundesanstalt für Geowissenschaften und Rohstoffe, Hannover, pp. 75–96.
- Metz, S., Trefry, J.H., Nelson, J.A., 1988. History and Geochemistry of a metalliferous sediment core from the Mid-Atlantic Ridge at 26N. *Geochim. Cosmochim. Acta* 52, 2369–2378.
- Mills, R., Elderfield, H., Thomson, J., 1993. A dual origin for the hydrothermal component in a metalliferous sediment core from the Mid-Atlantic Ridge. *J. Geophys. Res.* 98, 9671–9681.
- Moorby, S.A., Cronan, D.S., Glasby, G.P., 1984. Geochemistry of hydrothermal Mn-oxide deposits from the SW Pacific island arc. *Geochim. Cosmochim. Acta* 48, 433–441.
- Morton, J.L., Pohl, W., 1990. Magnetic anomaly identification in the Lau Basin and North Fiji Basin, southwest Pacific Ocean. In: Von Stackelberg, U., Von Rad, U. (Eds.), *Geological Evolution and Hydrothermal Activity in the Lau and North Fiji Basins Southwest Pacific Ocean*. Geologische Jahrbuch Reihe D, Heft 92, 93–108.
- Morton, J.L., Sleep, N.H., 1985. Seismic reflections from a Lau Basin magma chamber. In: Scholl, D., Vallier, T. (Eds.), *Geology of Offshore Resources of Pacific Island Arcs-Tonga Region*. Circum-Pacific Council for Energy and Mineral Resources. Earth Sci. Ser. vol. 2, 441–453.
- Mottl, M.J., Seewald, J.S., Wheat, C.G., Tivey, M.K., Michael, P.J., Proskurowski, G., McCollom, T.M., Reeves, E., Sharkey, Jessica, You, C.-F., Chan, L.-H., Pichler, T., 2011. Chemistry of hot springs along the Eastern Lau Spreading Center. *Geochim. Cosmochim. Acta* 75, 1012–1038.
- Pichler, T., Veizer, J., 1999. Precipitation of Fe(II) oxyhydroxide deposits from shallow-water hydrothermal fluids in Tutum Bay, Ambitle Island, Papua New Guinea. *Chem. Geol.* 162, 15–31.
- Pichler, T., Veizer, J., 2004. The precipitation of aragonite from shallow-water hydrothermal fluids in a coral reef, Tutum Bay, Ambitle Island, Papua New Guinea. *Chem. Geol.* 207, 31–45.
- Pichler, T., Nelson, E.P., Ridley, W.L., 1999. Low-temperature alteration of dredged volcanics from the Southern Chile ridge: additional information about early stages of seafloor weathering. *Mar. Geol.* 159, 272–285.
- Schaule, B.K., Patterson, C.C., 1981. Lead concentrations in the northeast Pacific: evidence for global anthropogenic perturbations. *Earth Planet. Sci. Lett.* 54, 97–116.
- Sinha, M.C., 1995. Segmentation and rift propagation at the Valu Fa Ridge, Lau Basin: evidence from gravity data. *J. Geophys. Res.* 100, 15025–15043.
- Stüben, D., Eddine, T.N., McMurtry, G.M., Scholten, J., Stoffers, P., Zhang, D., 1994. Growth history of a hydrothermal silica chimney from the Mariana backarc spreading center (southwest Pacific, 18°13′N). *Chem. Geol.* 113, 273–296.
- Sun, S.S., McDonough, W.F., 1989. Chemical and isotopic systematics of oceanic basalts: implications for mantle composition and processes. In: Saunders, A.D., Norry, M.J. (Eds.), *Magmatism in the Ocean Basins*. Geol. Soc. Special Publication 42, 313–345.
- Sun, Z.L., Zhou, H.Y., Yang, Q.H., Li, J., Yin, X.J., Li, J.W., submitted for publication. Formations of Fe–Si–Mn oxides and phyllosilicate in hydrothermal vent systems: example of Valu Fa Ridge in Lau back-arc basin. *J. Asian Earth Sci.*
- Takai, K., Nunoura, T., Ishibashi, J., Lupton, J., Suzuki, R., Hamasaki, H., Ueno, Y., Kawagucci, S., Gamo, T., Suzuki, Y., Hirayama, H., Horikoshi, K., 2008. Variability in the microbial communities and hydrothermal fluid chemistry at the newly discovered Mariner hydrothermal field, southern Lau Basin. *J. Geophys. Res.* 113, G02031. doi:10.1029/2007JG000636.
- Taylor, B., Zellmer, K., Martinez, F., Goodliffe, A.M., 1996. Sea-floor spreading in the Lau back-arc basin. *Earth Planet. Sci. Lett.* 144, 35–40.
- Tivey, M.K., Craddock, P., Seewald, J., Ferrini, V., Kim, S., Mottl, M., Sterling, A., Reysenbach, A.-L., Wheat, C.G., and the TUI05MV Scientific Party, 2005. Characterization of six vent fields within the Lau Basin. *Eos Trans. AGU*, 86 (52), Fall Meeting Suppl. (Abstract T31A-0477).
- Van de Flierdt, T., Frank, M., Halliday, A.N., Hein, J.R., Hattendorf, B., Günther, D., Kubik, P.W., 2004. Tracing the history of submarine hydrothermal inputs and the significance of hydrothermal hafnium for the seawater budget – a combined Pb–Hf–Nd isotope approach. *Earth Planet. Sci. Lett.* 222, 259–273.
- Varnavas, S.P., 1988. Hydrothermal metallogenesis at the Wilkes fracture zone—East Pacific rise intersection. *Mar. Geol.* 79, 77–104.
- Von Stackelberg, U. and Shipboard Scientific Party, 1988. Active hydrothermalism in the Lau back-arc basin (SW Pacific): first results from SONNE 48 cruise (1987). *Mar. Mining* 7, 431–442.
- Wiedicke, M., Collier, J.S., 1993. Morphology of the Valu Fa spreading ridge in the southern Lau Basin. *J. Geophys. Res.* 98, 11769–11782.
- Woodhead, J.D., Volker, F., McCulloch, M.T., 1995. Routine Pb isotope determinations using a ²⁰⁷Pb–²⁰⁴Pb double spike, a long-term assessment of analytical precision and accuracy. *Analyst* 120, 35–39.